A Method of Stall and Surge Prediction in Axial Compressors Based on Three-Dimensional Body-Force Model

Hanxuan Zeng
Turbomachinery Laboratory,
State Key Laboratory of Automotive Safety and Energy,
Tsinghua University,
Beijing 100084, China
e-mail: zenghx16@mails.tsinghua.edu.cn

Xinqian Zheng[1]
Department of Aerodynamics and Thermodynamics,
Institute for Aero Engine & Turbomachinery Laboratory,
State Key Laboratory of Automotive Safety and Energy,
Tsinghua University,
Beijing 100084, China
e-mail: zhengxq@tsinghua.edu.cn

Mehdi Vahdati
Department of Mechanical Engineering,
Imperial College London,
London SW7 2AZ, UK
e-mail: m.vahdati@imperial.ac.uk

The occurrence of stall and surge in axial compressors has a great impact on the performance and reliability of aero-engines. Accurate and efficient prediction of the key features during these events has long been the focus of engine design processes. In this paper, a new body-force model that can capture the three-dimensional and unsteady features of stall and surge in compressors at a fraction of time required for URANS computations is proposed. To predict the rotating stall characteristics, the deviation of local airflow angle from the blade surface is calculated locally during the simulation. According to this local deviation, the computational domain is divided into stalled and forward flow regions, and the body-force field is updated accordingly; to predict the surge characteristics, the local airflow direction is used to divide the computational domain into reverse flow regions and forward flow regions. A single-stage axial compressor and a three-stage axial compressor are used to verify the proposed model. The results show that the method is capable of capturing stall and surge characteristics correctly. Compared to the traditional fully three-dimensional URANS method (fRANS), the simulation time for multistage axial compressors is reduced by 1–2 orders of magnitude.
[DOI: 10.1115/1.4053103]

1 Introduction

Axial compressor is a key component in aero-engines. The problem of aerodynamic instability in axial compressors greatly affects the performance and reliability of the whole engine. Aerodynamic instabilities in axial compressors can be mainly divided into two categories, namely, rotating stall and surge. Rotating stall occurs with single or several stall cells covering a few blade passages. The existence of stall cells not only limits the pressure rise of compressors but also leads to structural fatigue, which results in costly maintenance or even engine grounding and thus, loss in revenue. Surge is an unstable flow pattern of the complete compression system consisting of the compressor itself, the piping system, and the throttling devices. Surge in a high-speed compressor can lead to violent disruption of the flow, damage to the structure, and eventually engine shutdown. Since these two kinds of aerodynamic instabilities are both destructive, it is crucial to carry out in-depth studies estimating the loadings during these events, so as to avoid possible in-service failures.

However, aerodynamic instabilities are rather complex, such as the typical three-dimensional and unsteady features, which are represented by the rotation of stall cells and the evolution of part-span reverse flow. It requires not only sufficient time-resolution but also three-dimensional spatial resolution (circumferential, radial, and axial) modeling to resolve and understand these flow phenomena and then, the overpressure and hence the loadings can be estimated. Considering the risks and high costs of experimental research and the difficulty in detailed flow-field measurement, alternative methods are required. Computational fluid dynamics simulations provide an alternative and economical way to further understand the compressor behavior during surge and stall. However, simulations of stall and surge by using fully unsteady Reynolds averaged Navier–Stokes (fRANS) require full-annulus grids, small time-steps, and long physical times. For typical multistage axial compressors used in aero-engines, it may take several months to obtain the results, which is unacceptable during design iterations. It is therefore of great importance to develop a method that can both predict the three-dimensional and unsteady features of stall and surge and reduce the simulation time significantly.

After decades of research, a series of reduced-order models have been developed to predict the aerodynamic instability of axial compressors, such as lumped-parameter models, actuator-disk models, and body-force models. Lumped-parameter model simplifies the components of an engine that is related to stall and surge into a dynamic system featuring plenum and pipe. Using time-marching methods, the computational cost of obtaining a solution is in the order of minutes. However, this model cannot resolve the flow distribution inside the compressor and can only provide a preliminary description of the overall characteristics [1,2]. Actuator-disk model has a similar problem as it simplifies the compressor to an actuator disk [3]. Hence, it can predict the number and the rotational speed of stall cells, but the flow distribution in radial and axial directions is not obtainable. To capture three-dimensional flow features, body-force model was proposed [4]. In this model, the effects of compressor blades are replaced by a spatially distributed body-force field. Because this model has three-dimensional grid resolution, it can provide a more detailed flow field. Body-force model was initially used to simulate the effects of inlet distortion, but in recent years, body-force model has started to emerge in the simulation of stall and surge [5–7]. The modeling of body-force is accomplished by calculating the body-force fields under different flow conditions and switching between them using predefined stall and surge criteria.

The first problem in applying body-force model to the simulation of aerodynamic instability is how to construct the body-force field. This is also the same for conventional body-force models dealing with stable flow conditions. At present, two main types are used: direct method and indirect method (feedback method). The direct method associates the body-force field with the compressor inlet mass flow rate and operating speed [8,9]. Based on pre-acquired data, which is limited to several operating points with different mass flow rates and speeds, a polynomial curve fit is used to obtain the body-force fields at any arbitrary operating points by interpolation and extrapolation. The pre-acquired data

[1]Corresponding author.
Manuscript received March 20, 2021; final manuscript received October 19, 2021; published online January 4, 2022. Assoc. Editor: Damian M. Vogt.

can either be derived from the experimental measurements or simulations at different levels [10]. The calculation of body-force field is rather straightforward using this method. However, because a fitting method is used and the data to be fitted originate from a compressor with specific design, the versatility of the model parameters are quite limited. Besides, the direct method is not valid for simulations of aerodynamic instabilities because no steady-state flow field data can be obtained across the surge/stall boundary and extrapolation across the stall boundary can generate large errors. The indirect method adopts the idea from feedback control. In this method, an error term representing the difference between the current flow field and the target flow field is used to "correct" the local flow. It is assumed in this method that the direction of airflow is consistent with the direction of a "virtual" blade when a steady-state is reached (i.e., slip boundary condition) and this "virtual" blade essentially represents the direction of the target velocity field. The local deviation angle [11,12] and the deviation velocity [13,14] are commonly used as error terms (the latter one is defined by the component of actual velocity normal to the target velocity). The key to the indirect method is the prediction of target velocity fields. For design conditions, a reasonable approximation is to set the target velocity tangent to the camber surface; thus, the error term is reduced to the deviation of the flow from the blade surface [11,12]. For off-design conditions, a common practice is to use deviation models to correlate the incidence angle and the deviation angle. By combining the distribution of blade metal angle, the target velocity field under different incidence angles can be found. Although the deviation models were quantified after the trailing edge, they are used in this paper to be computed all along the blade by assuming a continuous variation from the leading edge to the trailing edge. Since deviation models are calibrated using extensive test data, the versatility of the indirect methods improves over the direct methods.

Based on the constructed body-force, special treatments are needed to model aerodynamic instabilities. Traditionally, body-force model is used to simulate steady-state flow or flow with small distortions with the operating points mostly located on the forward flow range. For such flows, empirical correlations are well-established as there are no regions with large separated flow or reversed flow; thus, the same model parameters can be used at all circumferential and radial locations. However, for the simulation of stall and surge, the flow at different locations can either be unaffected (forward), separated (stalled), or reversed (see Fig. 1). Therefore, using the same model parameters cannot correctly model the formation and evolution of different flow features. In recent years, the body-force model has drawn interest among researchers and several attempts in modeling surge and stall have been made. Longley [5] modeled surge transient using body-force model for the first time. The forward and reverse flow conditions are modeled separately without considering their coexistence. The switching between the two flow conditions was realized based on the stage loss coefficient. Therefore, only the overall compressor performance was used to model the surge transient while the body-force model itself was capable of resolving the three-dimensional flow. Based on the concept of "virtual blade passage," Righi [6,7] further applied the body-force model to both stall and surge simulation of multistage axial compressors. In this method, the stall or surge criterion was applied to each "virtual passage" to identify the flow conditions instead of using a single parameter obtained from the overall stage performance. However, the derivation of body-force models was based on the idea of "infinite number of blades." Thus, how the "virtual passages" are divided is unclear. Also, for highly cambered and staggered blades, "virtual passages" will greatly deviate from the real blade passages.

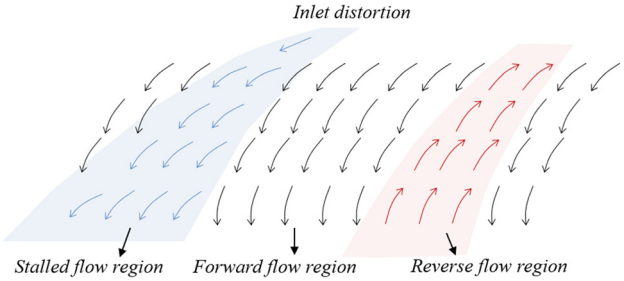

Fig. 1 Schematic of flow regions

To correctly model the formation and evolution of stalled and reverse flow regions with highly three-dimensional and unsteady flow features, a new body-force model is proposed. This model is based on the grid-local flow variables, so as to identify and simulate different flow features locally. This paper is divided into two main parts. The methodology is introduced first, including the governing equations, description of the solver and the methods for stall and surge modeling. Validation of the model is subsequently discussed on a single-stage axial compressor to validate its capability of capturing steady-state and rotating stall characteristics and a three-stage compressor is used to validate the capability of surge simulation.

2 Methodology

In body-force model, the blade region is assumed to consist of an infinite number of blades; thus, the compressor flow can be expressed by "locally axisymmetric" Euler equations. The blade force is modeled by a distributed body-force field, which is depicted by source terms. In this section, the governing equations of the body-force model and special treatments for different flow regions are introduced first, followed by a method of switching between different flow conditions based on the local flow variables.

2.1 Governing Equations. The governing equations to be solved are the Euler equations with source terms in the absolute frame of reference

$$\frac{\partial(b\rho)}{\partial t} + \nabla \cdot (b\rho \mathbf{V}) = 0 \tag{1}$$

$$\frac{\partial(b\rho \mathbf{V})}{\partial t} + \nabla \cdot (b\rho \mathbf{V}\mathbf{V}) = -\nabla(bp) + b\mathbf{f} \tag{2}$$

$$\frac{\partial(bh_t)}{\partial t} + \mathbf{V} \cdot \nabla(bh_t) = b\mathbf{f} \cdot \mathbf{U} \tag{3}$$

where $\mathbf{V}$, ρ, p, h_t, and t are the velocity, static density, static pressure, total enthalpy, and time, respectively. $\mathbf{U}$ is the blade speed. $\mathbf{f}$ is the body-force per unit mass of fluid. b is the local blockage factor accounting for the blockage caused by the blade thickness and boundary layer and can be further rearranged into source terms [15]. Conventionally, $\mathbf{f}$ is divided into two parts: a turning force to control the flow expansion and a loss force to control the entropy generation. This decomposition can be justified by incorporating Gibbs equation

$$T\nabla s = \nabla h - \frac{1}{\rho}\nabla p \tag{4}$$

where T, h, and s are the static temperature, static enthalpy, and entropy. By combining Eqs. (2)–(4), it can be shown that

$$T\mathbf{V} \cdot \nabla s = -\mathbf{f} \cdot \mathbf{W} \tag{5}$$

where $\mathbf{W}$ is the velocity relative to the blade. Equation (5) states that only the component of the body-force in the direction of $\mathbf{W}$ will generate entropy, while its normal component will not. Therefore, a turning force $\mathbf{f}_\zeta$ is defined along $\boldsymbol{\zeta}$ and a loss force $\mathbf{f}_\eta$

is defined along $\boldsymbol{\eta}$, where ζ and $\boldsymbol{\eta}$ are the normal and tangential component of $\mathbf{W}$.

2.2 Body-Force Modeling of Different Flow Regions. Based on the governing equations described above, how to model the turning and loss forces, as well as different treatments applied to each flow region will be discussed in this section.

2.2.1 Body-Force Modeling. The turning force $\mathbf{f}_\zeta$ is modeled by two parts. The first part is modeled by using the indirect method to correct the flow direction according to the variation of target velocity field. Although the first part is the main part of the body-force, which controls the evolution of the local flow field, However, this term alone may cause the simulation to crash when the initial condition of the simulation is inappropriate (namely, dramatically different from a physical solution). Consequently, a second term is added to provide a preliminary approximation, which is done more from a perspective of numerical robustness.

The indirect method [14] used for the first part has a generalized form of

$$f = K_p W_n + K_I \int W_n dt + K_D \frac{dW_n}{dt} \tag{6}$$

$$W_n = \mathbf{W} \cdot \mathbf{n} \tag{7}$$

where $\mathbf{n}$ is the unit vector normal to the local target velocity. The target velocity field is a virtual velocity field that is predicted at different incidence angle conditions based on the deviation angle (calculated using a deviation model) and the blade metal angle distribution. Therefore, W_n represents the difference between the relative velocity and the target velocity. Since the direction of target velocity takes into account the effect of both the blade geometry and local flow separation, W_n can be used as an error term for the feedback process. K_p, K_I, and K_D are the gain factors. They are acting to minimize the difference between the actual flow velocity and the target flow velocity. And the force constructed by them can be considered as a restoring force. K_p, K_I, and K_D depict how the error term is connected to the restoring force, i.e., proportional, integral, and differential. The first two terms in Eq. (6) are commonly used in the open literature [5,14]. The authors have found that for off-design conditions, the second term will create a discontinuity across the inlet plane of the blade region, which causes abrupt change of entropy. The second term is therefore not used in the present work. Equation (8) shows the final form of the indirect force used

$$f_{\zeta,1} = K_n \cdot \rho \frac{W_m \cdot W_n}{s \cdot \cos\beta} \tag{8}$$

where K_n is the gain factor, $\mathbf{m}$ is the streamwise unit vector, and $\boldsymbol{W}$ is the relative velocity projected to the streamwise surface as shown in Fig. 2. s and β are the blade pitch and blade metal angle, respectively. The definitions of $\boldsymbol{W}_\mathbf{n}$ and W_m are also shown in Fig. 2. Normally, larger values of blade pitch and smaller values of meridional velocity indicate lower stage loading. By including these two terms, the versatility of the gain factor is enhanced over different designs.

In the absence of the second term in Eq. (6), the value of gain factors K_n is adjusted to the degree that the actual velocity field converges to the target velocity field at the blade trailing edge in solving the steady characteristics of the compressor. This yields a range from 15 to 20. The same value is used for stall/surge simulations (same value is also used for both of the two cases in this paper). Since the gain factor K_n will also interfere with the dynamic response of the body-force field and consequently the dynamic response of the flow, further comparisons on the transient operation are provided in Sec. 3.2.

Equations for the second part of the turning force $\mathbf{f}_\zeta$ are derived from what was proposed by Longley [5]. Along with Eq. (8), the turning force is written as

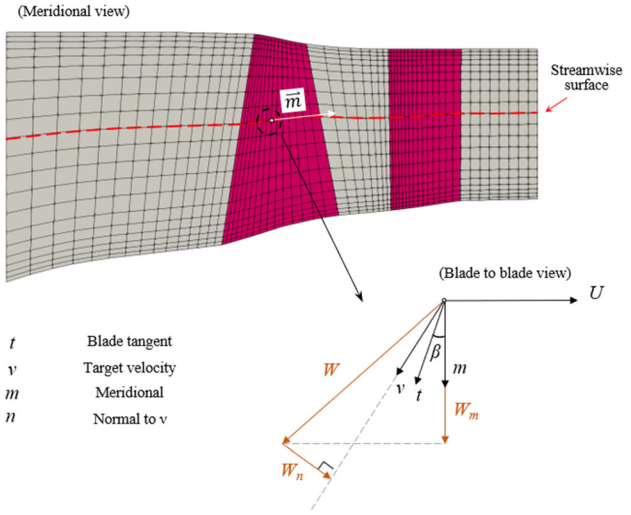

Fig. 2 Definition of the indirect body-force

$$f_\zeta = K_n \cdot \rho \frac{W_m \cdot W_n}{s \cdot \cos\beta} + \frac{\rho |\mathbf{W}|^2}{R} \tag{9}$$

$$\mathbf{f}_\zeta = f_\zeta \cdot \boldsymbol{\zeta} \tag{10}$$

$$W_m = \mathbf{W} \cdot \mathbf{m} \tag{11}$$

where R is the blade curvature.

The loss force $\mathbf{f}_\eta$ is modeled by two parts (as shown in Eq. (12)) to take into account both the surface friction loss and the secondary loss related to the adverse pressure gradient

$$f_\eta = K_{t1} \cdot \rho |\mathbf{W}|^2 + K_{t2} \cdot \rho \frac{\partial p}{\partial m} \frac{|\mathbf{U}|^2 |\mathbf{W}|}{|\mathbf{V}|^3} \tag{12}$$

$$\mathbf{f}_\eta = f_\eta \cdot \boldsymbol{\eta} \tag{13}$$

where K_{t1} and K_{t2} are functions of incidence angle and are calibrated based on the form of Carter's model [16].

2.2.2 Calculation of Target Velocity Field. The calculation of target velocity field is critical in the indirect method, which is used in the modeling of the turning force in Eq. (8). In the process of stall and surge, the flow field is not uniform, but consists of diverse flow regions, i.e., forward flow region, stalled flow region, and reverse flow region. For each region, calculation of the target velocity field is different.

For forward flow and stalled flow regions, the calculation of target velocity field is directly correlated to the incidence angle. By applying the deviation model, along with the distribution of blade metal angle from the leading edge to the trailing edge, the target velocity field can be calculated under different inflow conditions. For forward flow region, Cetin's model [17] is used to predict the nominal deviation angle δ^* and the deviation angle at different incidence angle conditions is calculated by using the Creveling's model [18]. Since most of the deviation models or their combinations are designed to predict the design and off-design conditions at the same time based on incidence angles, and the deviation angle also exists at design conditions, no special treatment is applied to distinguish between design and off-design conditions. For stalled flow region, Moses's model [19] is used to predict the deviation angle and hence the target velocity field. It should be noted that for new designs, especially for modern highly loaded stages, new deviation models are required, or alternatively, calibrating the current deviation model by several steady-state solutions from RANS simulations.

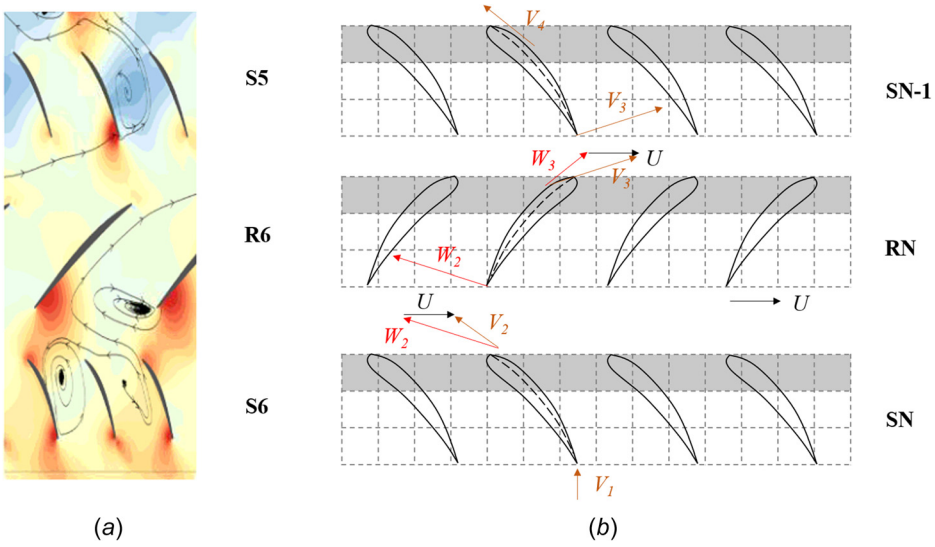

Fig. 3 Typical flow field and velocity diagram of the reverse flow condition: (*a*) pressure contour of the reverse flow condition (fRANS result) and (*b*) simplified velocity diagram (N represents the last stator)

For reverse flow regions,[2] Fig. 3(*a*) [20] shows the typical flow field during the reverse flow of surge transient. It can be seen that the "incidence angle" at the trailing edge of both rotor (dented by R6) and stator (denoted by S5) is large (nearly 90 deg) due to the reverse flow operation, and a separation vortex is formed close to the suction side of the blade. However, when the flow approaches the leading edge, the airflow near the pressure side follows the blade again, while the momentum of flow at the suction side is still low. Within the rotor–stator gap, the deviation angle is increased further due to the mixing of the flow from the pressure side and the suction side. Figure 3(*b*) simplifies this process in terms of velocity diagram. The mesh grid and the "virtual blade" are also shown by dashed and solid lines, respectively. Since the body-force model cannot differentiate between the two sides of the blade, only the flow close to the pressure side is modeled, which implies that the deviation angle at the blade leading edge can be set to zero in calculating the target velocity field. This is because the momentum of flow at the pressure side is dominant. Besides, the loss force is not active in this region. Loss is introduced naturally by setting the direction of turning force normal to the blade. In this case, the component of turning force in the direction of relative velocity is always negative and will generate entropy during the reverse flow conditions.

2.3 Switching Method for Rotating Stall and Surge Transients. In rotating stall and surge transients, different flow regions, i.e., forward flow region, stalled flow region and reverse flow region, may coexist at different axial, radial, and circumferential locations, which creates highly three-dimensional features. In conventional methods, which use small disturbance theory, it is assumed that the nonuniformity of the flow field does not affect the model itself. This implies that the modeling does not change according to the local flow features. However, in the case of rotating stall and surge featuring large disturbances, different flow regions should be modeled separately.

The key to solving this problem is how to identify different flow regions based on the local flow variables; thus, a corresponding appropriate model can be applied. It is noted that the local deviation of actual flow from the blade surface, namely, local deviation angle, reflects the magnitude of flow separation, and the increase of flow separation is directly related to the occurrence of stall. Besides, the reverse flow region can be identified by the flow direction right away. Therefore, based on the local flow angle and the blade metal angle, the computational domain can be grouped into different flow regions. The corresponding target velocity field and body-force field can be calculated according to Eq. (9) in Sec. 2.2.

The above treatment is drawn from the idea of a heuristic model used to predict the compressor performance curve under the condition of rotating stall [21]. Figure 4 illustrates how this model works in rotating stall and surge simulations. For the simulation of rotating stall, part of the computational domain is identified as stalled flow region, represented by operating point B with nearly zero mass flow rate. The unstalled region (or forward flow region, point A) experiences high mass flow rate and small incidence angle. Closing and opening the downstream throttle will cause the stalled region to expand or shrink. The compressor mass flow rate will decrease or increase accordingly from the original condition (point C in Fig. 4), while the pressure ratio remains unchanged. To achieve this idea, first a steady simulation is required, with a gradual decrease of the mass flow by adjusting the throttle coefficient, until the local incidence at the leading edge meets the critical incidence angle i_s defined by Herrig's model [22]

$$i_s = i^* + 1.5\left[10 + \frac{\theta(55-\beta_1)}{150}\right]\left(0.5 + 5.0\frac{t_b}{c}\right) \tag{14}$$

where θ, β_1, t_b, and c are the blade camber angle, inlet metal angle, maximum thickness, and chord, respectively. Afterward, a

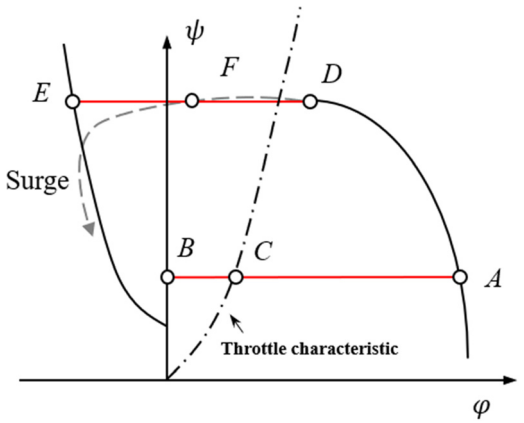

Fig. 4 Modeling of stall and surge based on the local flow variables (φ: flow coefficient, ψ: pressure rise coefficient)

[2]The definitions of leading/trailing edge are the same as those for forward flow conditions

local deviation angle field is extracted from the result (subtracting the blade metal angle from the actual flow angle), and is used as a threshold to judge at each mesh point if a local separation will appear or not, as is illustrated by the shadowed or the gray regions in Fig. 5, respectively. In this way, the stalled region is identified from the flow field and its evolution can be modeled locally. Finally, the body-force field is calculated and updated based on the region-averaged incidence angle using Eqs. (9)–(13). Similarly, during surge, this is done by tracking the flow direction at each mesh point. The reverse flow emerges naturally by overpressure or stall. After they are identified as reverse flow region (represented by operating point E in Fig. 4), the target velocity is updated correspondingly.

In practice, stalled flow region and reverse flow region may exist at the same time, in which case both the stall and reverse flow criteria are used. For multistage compressors, only the stage that has reached the stall limit is evaluated using the threshold for stall, while other stages are only evaluated by surge criterion (back-flow test). This is a reasonable approximation for abrupt surge cases because the stalled region turns into reverse flow region and expands in the axial direction so quickly that the process from stall to surge of other stages can be omitted. For rotating stall cases, this may underestimate the size of the stall cells.

2.4 Implementation and Numerical Control. Figure 6 illustrates the basic structure of the solver in terms of a flowchart. The solver is built based on OPENFOAM, which is a C++ toolbox for the development of customized numerical solvers and pre-/postprocessing utilities for general computational fluid dynamics [23]. Body-force is implemented as extra source terms in the governing equations. During preprocessing, apart from generating mesh, calculations of additional scalar and vector fields, which includes blade metal angle, thickness, curvature and predefined velocity fields, are performed. The predefined velocity fields are used to reduce the time needed for the calculation of target velocity fields during the simulation. The body-force main module corresponds to the content discussed in Secs. 2.2 and 2.3.

To deal with the compressor outlet flow during surge simulations, a new plenum-throttle boundary condition is implemented following the rules of OPENFOAM DLL. Governing equations are derived from the continuity equation and the energy equation of a homogeneous plenum, along with the throttle function. The plenum density ρ_p and temperature T_p are expressed by

$$V_p \cdot \frac{d\rho_p}{dt} = \dot{m}_c - \dot{m}_t \tag{15}$$

$$\rho V_p c_v \cdot \frac{dT_p}{dt} = \dot{m}_c c_p T_c - \dot{m}_t c_p T_p + (\dot{m}_c - \dot{m}_t) \cdot c_v T_p \tag{16}$$

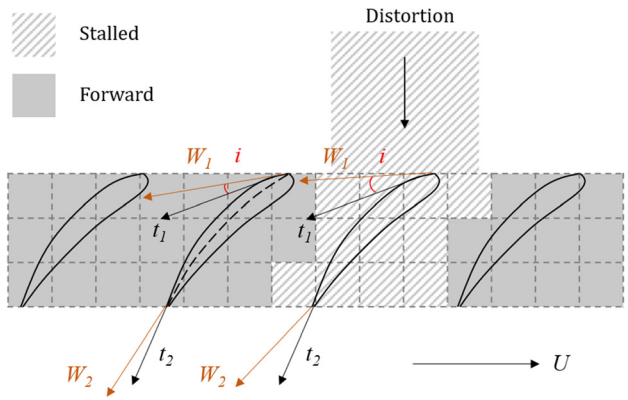

Fig. 5 Identification of forward flow region and stalled flow region based on local flow variables

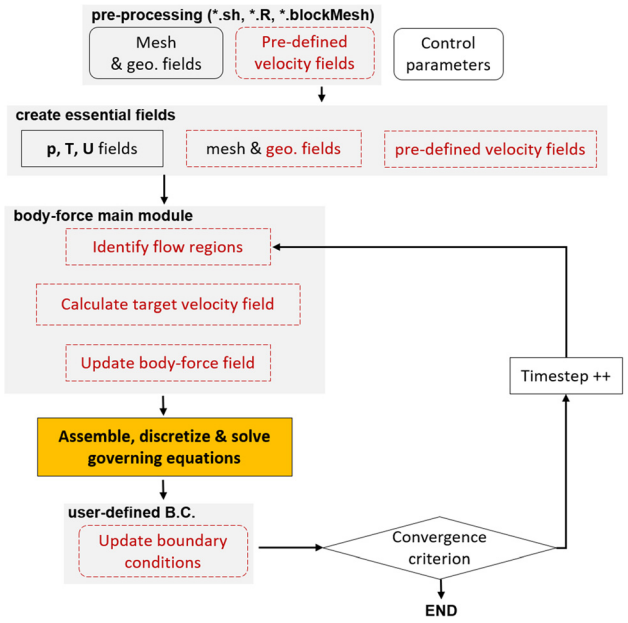

Fig. 6 Flowchart of the solver implementation (new modules for body-force model is shown dashed frames, others are modified based on existing modules)

where V_p is the plenum volume; $\dot{m}_c$ and $\dot{m}_t$ are the compressor outlet mass flow rate and throttle mass flow rate; c_v and c_p are the specific heat capacity. Similar treatments can also be found in Refs. [24] and [25]. The throttle mass flow rate is determined by the pressure difference between plenum and the ambient condition. In practice, only the plenum volume and the throttle coefficient are solver inputs. The final steady-state solution is controlled by throttle coefficient and is independent of plenum volume. At the inlet boundary, total pressure and total temperature are specified during forward flow and static pressure is specified during reverse flow.

Governing equations are solved explicitly in the time domain. Both the steady and unsteady (stall and surge) characteristics of the following two validation cases are obtained by unsteady simulations; thus, "steady" in this paper only refers to the final solution stops changing in time. The courant number is strictly limited below 0.1. The original solver adapted from OPENFOAM uses explicit time-stepping scheme; thus, the Courant–Friedrichs–Lewy number was set quite conservatively. Also, by referencing to the OPENFOAM documentations, the maximum courant numbers are set around 0.2; therefore, a small value is used in this paper mainly for the consideration of numerical robustness. The Kurganov central-upwind scheme is used in this solver to capture transonic flow regions [26]. Full annulus and structured mesh of a single-stage axial compressor for body-force simulation is shown in Fig. 7. The whole domain is divided into blade regions (which include both rotors and stators) and nonblade regions based on the locations of the blade leading edge and trailing edge. Since coarse grids are used, the simulation time are reduced by 1–2 orders of magnitude as compared to fRANS. The efficiency of the current model can be improved by using the implicit time-stepping schemes.

3 Model Validation

3.1 Validation of Rotating Stall Modeling. NASA rotor 67 [27] is selected as the test case in this paper. It is an undampered, low-aspect-ratio designed rotor. The design pressure ratio is 1.63 at a corrected mass flow rate of 33.25 kg/s. The design rotational speed is 16,043 r/min, which yields a tip speed of 429 m/s and inlet tip Mach number of 1.38. The rotor has 22 blades and the

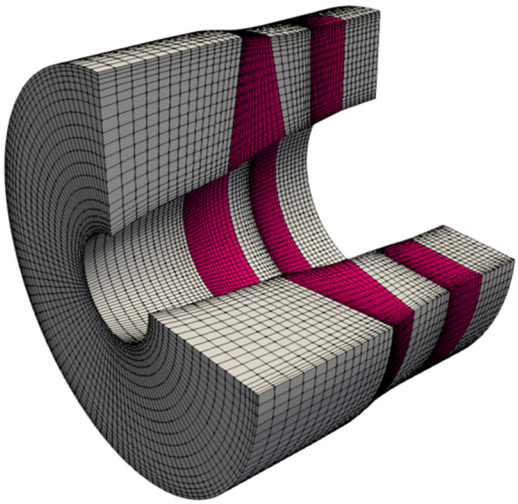

Fig. 7 Typical mesh of single-stage compressor used in body-force model

stator S67A has 34 blades. The experiments were carried out at the W8 single-stage compressor test facility at NASA Glenn Research Center. Comparison of the overall stage performance between body-force model results and test results are shown in Fig. 8, where the loss coefficient is tuned at the highest speed and is used for the remaining speeds. Good agreement is obtained, except that the predicted efficiency at 70% design speed is slightly lower than the test results. The differences at lower speeds may result from the fact that the Mach number effects are not included in the formulation of the loss force; thus, the error from the loss force increases with decreasing speeds. Another possible reason is the uncertainty of experimental measurements, since results from fRANS simulations also show underpredicted efficiency, especially for rotor alone [28].

Since only the measured overall performance is available, the results of fRANS simulations were used to investigate the capabilities of the body-force model for predicting the main features of the meridional flow field at both steady and rotating stall conditions. The fRANS results used for comparison were taken from Zhang's work [29]. These results were chosen as the Computational fluid dynamics code used for this study was validated extensively against measured data for both steady and unsteady conditions [30]. The Spalart–Allmaras turbulence model was used, which has been adjusted accordingly, and the resulting code was used in series of works [31,32]. A grid size study was performed to obtain an optimum mesh, which yielded a grid of 1×10^6 mesh points and a maximum y^+ of 10. Also, a time-step convergence study was performed and the setting of 400 time-steps/cycle (around 18 time-steps/passage) was selected.

To evaluate the capability of body-force model to predict the steady-state flow field, a near stall operating condition is simulated at 90% design speed. Static pressure and temperature contours are compared against the fRANS results in Fig. 9. The body-force model captures the radial (near points P1 and P2) and axial (near point P3) pressure gradient correctly, as well as the low-pressure region induced by the negative incidence at the stator inlet (near P4). The overall agreement is satisfactory, although at the tip region of rotor leading edge, a bow shock was well-captured by the fRANS simulation (near P5), while in body-force model, no shock front was observed. This can be attributed to the use of "virtual" blades as compared with the actual blades in fRANS. Furthermore, the temperature distribution is not predicted to the same level of accuracy as the pressure, which is due to the local loss generation estimated by Eq. (12). The development of boundary layer along the blade surfaces and end walls and the flow mixture cannot be fully resolved. An alternative way of using viscous body-force model [33] can be considered in the future.

Figure 10 shows the axial velocity contours at rotating stall simulations. Stall is triggered by both throttling the downstream valve and mis-staggering one of the rotor blades, which is similar to the strategy used in fRANS computation [28,29]. From Figs. 10(*a*) and 10(*b*), it can be seen at the blade tip that the stall cell is captured by both methods. For the body-force model, the circumferential extent of the stall cell is larger due to the absence of the blades. A streamwise cut at the center of stall cell is shown in Figs. 10(*c*) and 10(*d*). Both methods captured the accelerated flow at the near hub region caused by the blockage of the stall cell.

By evenly placing 6 numerical probes circumferentially at the rotor leading edge, time traces of axial velocity are compared in Fig. 11. It is clear that disturbances caused by the stall cell are rotating circumferentially. The predicted speed is 61% of the blade rotational speed for body-force model, and 63% for fRANS. According to the classic explanation of rotating stall by Emmons [34], the existence of stall cells causes flow blockage in the blade passage and spillage at the passage inlet. This increases the flow incidence at the upstream (circumferentially) passage and decreases the flow incidence at the downstream passage. Thus, the stall cell will shift circumferentially upstream. In this explanation, the redistribution of compressor flow due to the existence of stall cells and the consequent change of incidence angle around the circumference is the main cause of this rotating stall phenomenon. In the body-force model, although the blades are not simulated directly, the flow redistribution is captured at either side of the stall cell because the update of target velocity field is partly driven by the change of region-averaged incidence angle. Also, this redistribution migrates with stall cells; thus, the phenomenon of rotating stall is correctly modeled.

The above validation is a good indication that the model is capable of predicting the stall phenomenon correctly. However, since the model simplifies the blade-to-blade flow to a locally

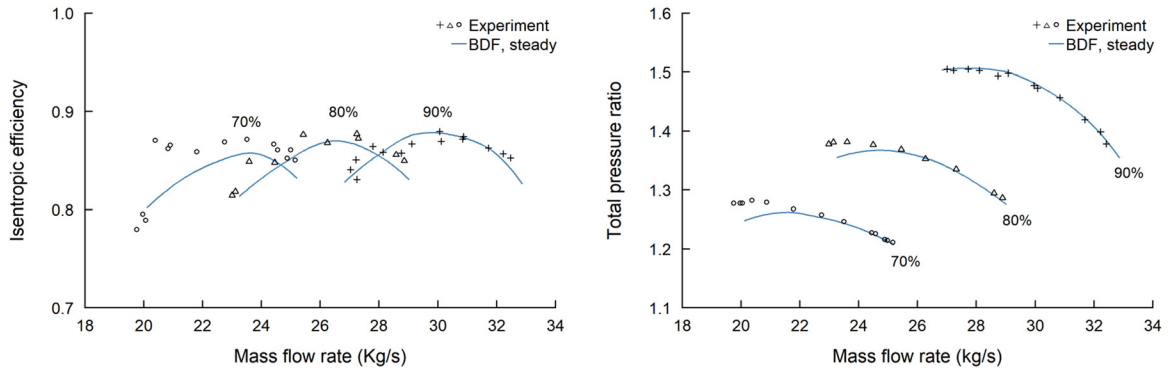

Fig. 8 Performance map of stage 67: (*a*) mass flow rate versus efficiency and (*b*) mass flow rate versus pressure ratio

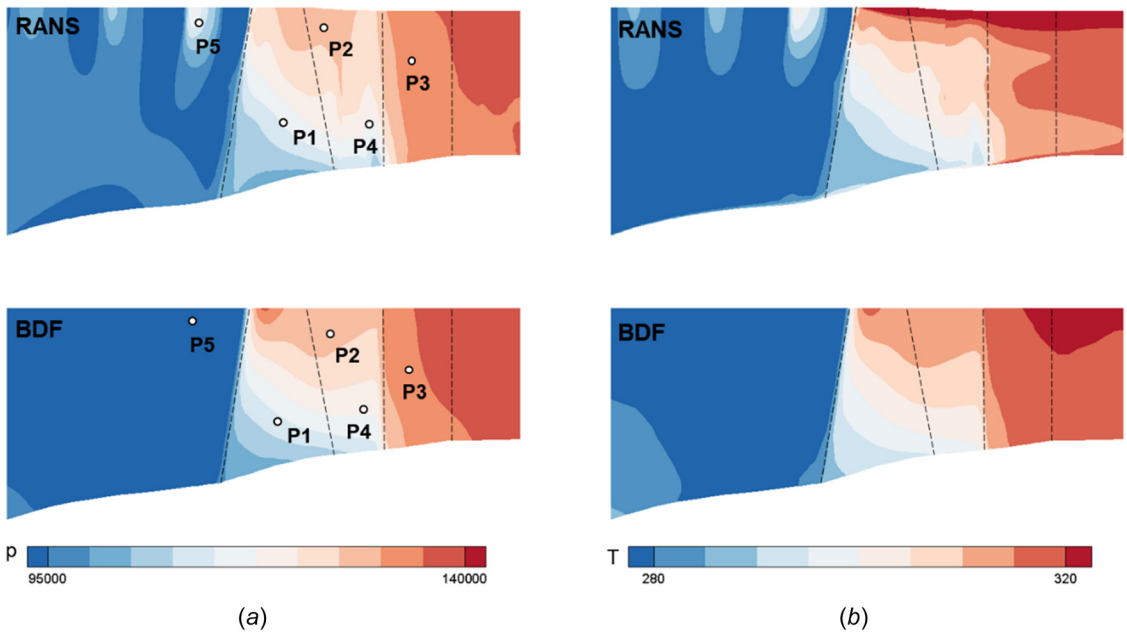

Fig. 9 Flow field comparison of stage 67, 90% design speed: (*a*) static pressure contour at near stall condition and (*b*) static temperature contour at near stall condition

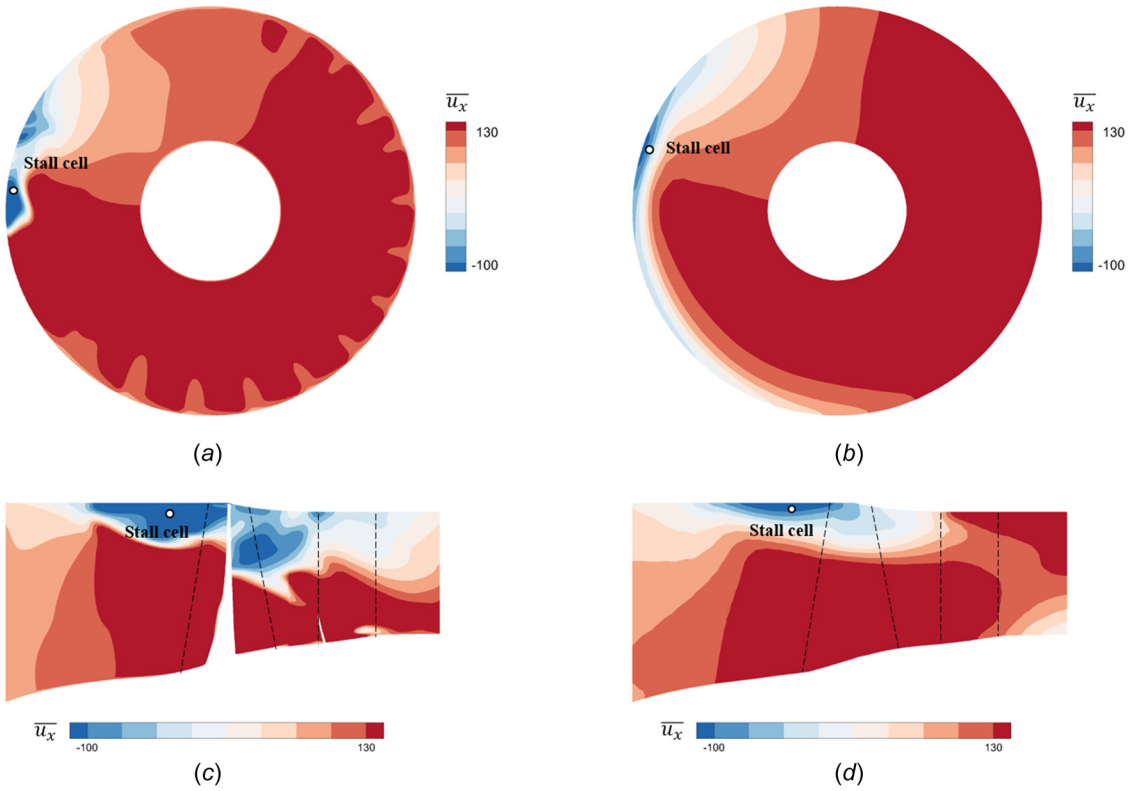

Fig. 10 Axial velocity contour of stage 67 at rotating stall condition, 90% design speed: (*a*) fRANS, rotor inlet view, (*b*) BDF, rotor inlet view, (*c*) fRANS, meridional view, and (*d*) BDF, meridional view

axisymmetric flow, detailed flow structures, such as leakage flow (closely related to the stall inception), are not obtainable. Moreover, the size of stall cells should be larger than at least one blade pitch, which is the case for the geometry considered. Therefore, it is expected that the proposed model can capture large-scale in-stall features of rotating stall. More cases are needed for comprehensive validation.

3.2 Validation of Surge Modeling. To further demonstrate the capabilities of the proposed algorithm, surge simulation of a three-stage axial compressor is considered next. In Ref. [35], two designs with different reactions were tested by Gamache, and the moderate reaction design is compared against the body-force results in Fig. 12. During the test, a centrifugal exhaust blower was installed at the compressor outlet along with an adjustable conical nozzle to obtain the reverse-flow characteristics. A system pressure loss analysis was also conducted to evaluate the capability of the exhaust blower to sustain the reverse-flow condition. For the body-force model, this is achieved by modifying the boundary conditions. Total pressure and total temperature were given at the

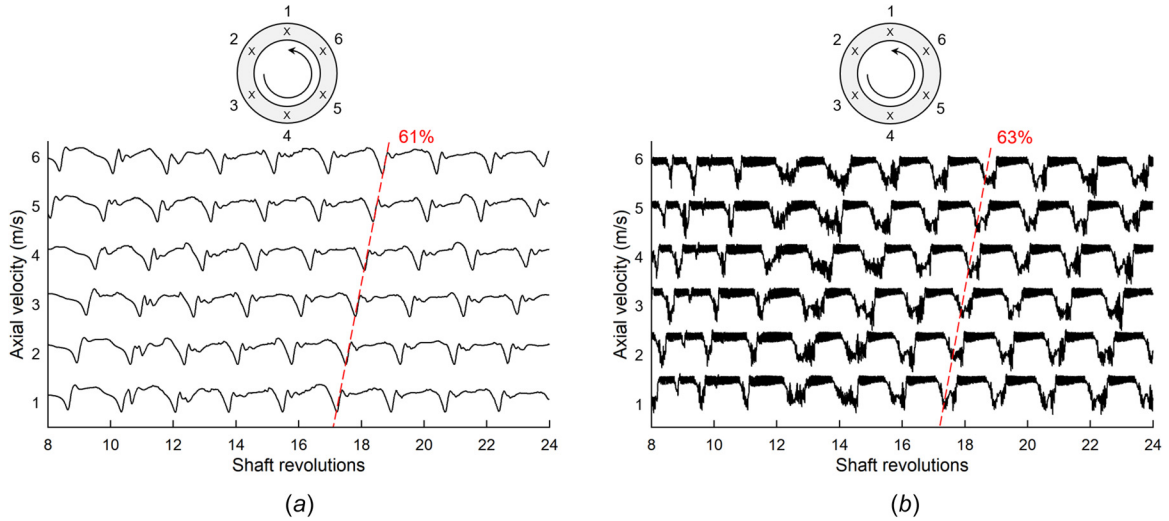

Fig. 11 Time traces of axial velocity of six upstream probes: (*a*) BDF result (*b*) fRANS result

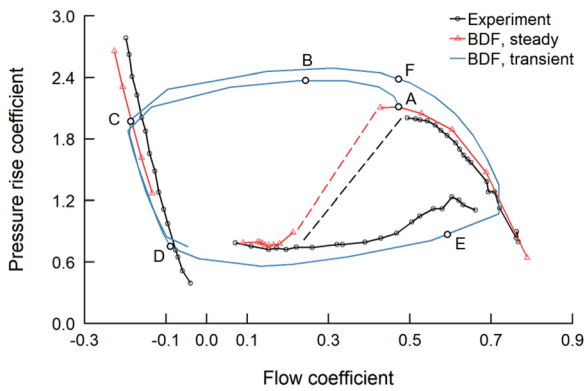

Fig. 12 Simulation results and test results of the three-stage compressor

compressor outlet to imitate the outlet condition of the exhaust blower, while static pressure was set as the inlet boundary condition. The computational domain for body-force model has 40, 147, and 20 elements in the circumferential, axial and spanwise directions, respectively. This yields 0.12×10^6 mesh cells. It can be seen from Fig. 12 that the body-force model can capture both forward and reverse flow characteristics with good precision. The surge simulation (labeled ABCDEF) is also presented in Fig. 13 showing the evolution of flow and pressure coefficients versus time. A slight overshoot is observed at the beginning of surge, because the initial condition is not exactly located at the surge line. Although no surge data are available from the test, it is noted that the body-force model captures the switching of transient operating point between the positive and negative characteristic curves in Fig. 12 and the transient operating point is close to the steady characteristics. Additionally, the axial pressure gradient in the compressor is at its minimum when the compressor starts to recover, which has already been observed in surge simulations by URANS [20,36]. Simulation results with different gain factors within the recommended range are also combined and shown in Fig. 13(*b*). Larger gain values increase the pressure overshoot from the steady characteristics slightly at the beginning of surge. This mostly results from enhanced dynamic response of the turning force and the abrupt change of the flow field (from forward flow to back flow). The effect is greatly weakened at more progressively developing flow conditions afterward as shown at the beginning of the recovery phase. Therefore, the main features of surge including the timescales are unaffected.

Figure 14(*a*) shows the mesh in a meridional view. Blade regions and nonblade regions are marked by different colors, respectively. Recalling that a switching method is used to model the compressor aerodynamic instabilities based on the local flow variables, Fig. 14(*c*) shows the identified flow regions visually and how the flow field reacts to them. Considering R1 in Fig. 14(*a*) as an example, the variation of averaged incidence angles for each

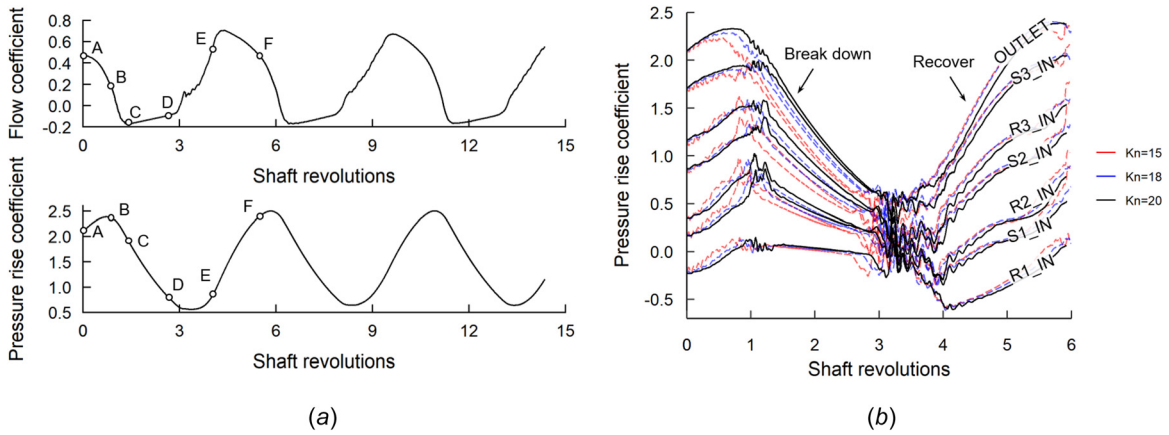

Fig. 13 Transient flow quantities at several stations of the three-stage compressor (body-force method results): (*a*) variation of flow and pressure rise coefficients at the compressor outlet and (*b*) variation of pressure rise coefficient at the inlet and outlet of each blade row

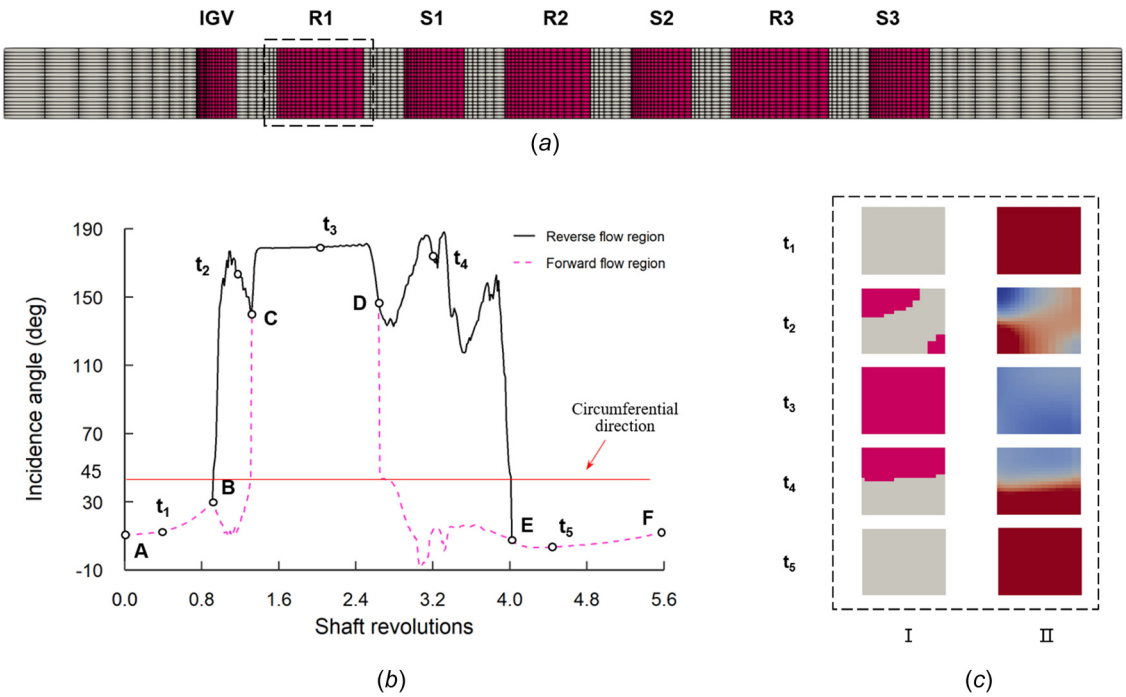

Fig. 14 The role of switching method in the surge simulation: (*a*) mesh view of three-stage compressor, (*b*) averaged incidence angle of reverse flow and forward flow region, and (*c*) evolution of reverse flow region (I) and axial velocity contour (II), R1 in (a)

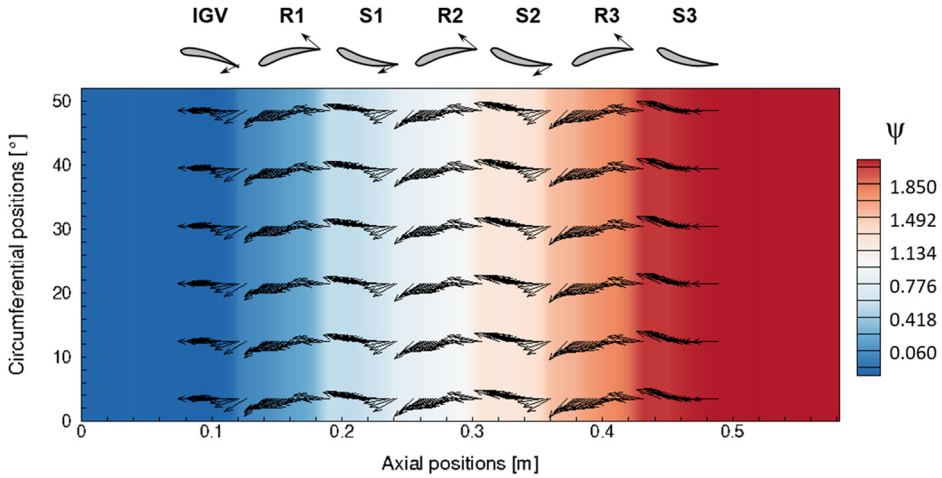

Fig. 15 Pressure rise coefficient contour with relative velocity vectors of three-stage axial compressor (flow coefficient: 0.2, 50% span)

region of R1 during one surge cycle are compared in Fig. 14(*b*). For surge, the formation and evolution of two main flow regions are critical, i.e., forward flow region and reverse flow region. Therefore, the entire cycle is divided into five segments in Fig. 14(*b*) by four points: the occurrence of reverse flow region (B), the vanishing of forward flow region (C), the re-occurrence of forward flow region (D), and the vanishing of reverse flow region (E). In each segment, one operating point is picked to show the evolution of the identified flow regions (i.e., forward and reverse flow) in Fig. 14(*c*) (t_1 to t_5): on the left-hand side, the identified forward and reverse flow region are shown by two different colors, while the axial velocity contours are shown on the right-hand side. At point t_2, part-span reverse flow is observed (similarly at point t_4). Hence, the two regions of flow have different incidence angles and are updated correspondingly. The horizontal line marks the circumferential direction and any points above it denote reverse flow. However, the incidence angle begins to differ since point B, instead of right on the horizontal line. This shows a sudden flow reversal marking the surge inception. After that, due to the rapid expansion of reverse flow region, the incidence angle of forward flow region decreases slightly and then increases abruptly due to the instantaneous collapse of adverse pressure gradient throughout the compressor. From point D, the axial pressure gradient in the compressor starts to build up, and the forward flow region appears again, while the reverse flow region shrinks gradually. It is because the model identifies the flow regions correctly according to the local flow condition that the switching of the positive/negative flow characteristics can be simulated correctly.

Figure 15 shows the pressure rise coefficient contour along with the relative velocity vectors at point t_3. Since the flow field is circumferentially uniform, only a 50-deg sector is shown. The "virtual blades" of each blade row are plotted with the sketched flow vectors at the trailing edge. The result is consistent with the flow features near the blade pressure side as shown in Fig. 3. It is thus indicated that the simplified formulation of the reverse flow condition is reasonable.

4 Conclusion

In this paper, a new body-force model for the prediction of stall and surge in axial compressors is proposed. Two open cases are used to validate the model. Main conclusions are as follows:

(1) A switching method based on the local flow variables is proposed for modeling the typical three-dimensional flow features, which occur during stall and surge. By monitoring the deviation angle between the local airflow and the blade surface during the simulations, the computational domain is grouped into forward, stalled, and reverse-flow regions. Corresponding formulations are applied to each region to calculate the target velocity field; hence, the body-force field is updated. Because this method uses grid-local variables, it can identify and simulate local flow features to a great extent.
(2) The model is applied to a single-stage axial compressor. The simulation of steady-state flow field is validated by comparing against fRANS results and measured data. Further analysis shows that the new model can simulate rotating stall, and the radial location and the rotational speed of the stall cell are predicted with good precision.
(3) The capability of surge simulation is examined for a three-stage axial compressor. Body-force model captures the switching of transient operating point between the positive and negative characteristic curves accurately, and the transient operating point was found to be close to the compressor steady characteristics. When the compressor starts to recover from surge, the pressure gradient is at its minimum, which is also observed in URANS simulations of multi-stage axial compressors.

Acknowledgment

The authors would like to express special thanks to the colleagues from Imperial College London: Dr. Wenqiang Zhang provided the fRANS results of Stage 67, Dr. Xiao He and Dr. Fanzhou Zhao shared valuable insights during the development of the model.

Funding Data

- National Science and Technology Major Project (2017-II-0004-0016; Funder ID: 10.13039/501100013076).
- Natural Science Foundation of China (Grant No. 51876097; Funder ID: 10.13039/501100001809).

Nomenclature

b = blockage factor
c = chord length
E = total energy
f = body-force
h = static enthalpy
i = incidence angle
K = gain factor
m = mass flow rate, streamwise unit vector
n = unit vector normal to the target velocity
p = static pressure
R = blade curvature
s = entropy, pitch
t = unit vector tangent to the target velocity
T = static temperature
t_b = maximum blade thickness
U = blade velocity
V = absolute velocity, volume
W = relative velocity

Greek Symbols

β = blade angle
δ = deviation angle
ζ = unit vector normal to the relative velocity
η = unit vector tangent to the relative velocity, isentropic efficiency
θ = camber
π = total to total pressure ratio
ρ = static density
φ = flow coefficient $\dot{m}/\rho UA$
Ψ = pressure rise coefficient $(p - p_{\text{ref}})/\frac{1}{2}\rho U^2$

Subscripts

c = compressor
m = streamwise
n = normal of target velocity
p = plenum
ref = reference condition
s = stall
t = tangent of target velocity, throttle
ζ = normal of relative velocity
η = tangent of relative velocity
1 = flow inlet
2 = flow outlet

Superscripts

$*$ = nominal condition
$\bar{}$ = corrected by averaged value of the inlet plane

Acronyms

*f*RANS = fully three-dimensional URANS method
URANS = unsteady RANS method

References

[1] Moore, F. K., and Greitzer, E. M., 1986, "A Theory of Post-Stall Transients in Axial Compression Systems: Part I—Development of Equations," ASME J. Eng. Gas Turbines Power, **108**(1), pp. 68–76.
[2] Greitzer, E. M., and Moore, F. K., 1986, "A Theory of Post-Stall Transients in Axial Compression Systems: Part II—Application," ASME J. Eng. Gas Turbines Power, **108**(2), pp. 231–239.
[3] Spakovszky, Z. S., 2000, "Applications of Axial and Radial Compressor Dynamic System Modeling," Doctoral dissertation, Massachusetts Institute of Technology, MA.
[4] Gong, Y., Tan, C. S., Gordon, K. A., and Greitzer, E. M., 1999, "A Computational Model for Short-Wavelength Stall Inception and Development in Multistage Compressors," ASME J. Turbomach., **121**(4), pp. 726–734.
[5] Longley, J. P., 2007, "Calculating Stall and Surge Transients," ASME Paper No. GT2007-27378.
[6] Righi, M., Pachidis, V., and Könözsy, L., 2018, "Three-Dimensional Through-Flow Modelling of Axial Flow Compressor Rotating Stall and Surge," Aerosp. Sci. Technol.,, **78**(2018), pp. 271–279.
[7] Righi, M., Pachidis, V., Könözsy, L., Zhao, F., and Vahdati, M., 2020, "Three-Dimensional Low-Order Surge Model for High-Speed Axial Compressors," GPSS Global Power and Propulsion Chania 20 Technical Conference, Chania, Greece, Sept. 7–9, GPPS Paper No. GPPS-CH-2020-138.
[8] Chima, R. V., 2006, "A Three-Dimensional Unsteady CFD Model of Compressor Stability," ASME Paper No. GT2006-90040.
[9] Kiwada, G., 2008, "Development of a Body-force Description for Compressor Stability Assessment," Doctoral dissertation, Massachusetts Institute of Technology, MA.
[10] Patel, A. A., 2009, "Assessment of a Body-force Representation for Compressor Stability Estimation," Doctoral dissertation, Massachusetts Institute of Technology, MA.
[11] Hall, D. K., Greitzer, E. M., and Tan, C. S., 2017, "Analysis of Fan Stage Conceptual Design Attributes for Boundary Layer Ingestion," ASME J. Turbomach., **139**(7), p. 071012.
[12] Akaydin, H. D., and Shishir, A. P., 2017, "Implementation of a Body-Force Model in OVERFLOW for Propulsor Simulations," AIAA Paper No. AIAA-2017-3572.
[13] Cao, T., Hield, P., and Tucker, P. G., 2017, "Hierarchical Immersed Boundary Method With Smeared Geometry," J. Propul. Power, **33**(5), pp. 1151–1163.
[14] Watson, R., Cui, J., Ma, Y., Tyacke, J., Vadlamani, N. R., Alam, M. F., and Dai, Y., 2017, "Improved Hierarchical Modelling for Aerodynamically Coupled Systems," ASME Paper No. GT2017-65223.
[15] Kottapalli, A. P., 2013, "Development of a Body-Force Model for Centrifugal Compressors," Doctoral dissertation, Massachusetts Institute of Technology, MA.
[16] Carter, A. D. S., Andrews, S. J., and Shaw, H., 1950, "Some Fluid Dynamic Research Techniques," Proc. Inst. Mech. Eng., **163**(1), pp. 249–263.

[17] Cetin, M., Ucer, A. S., Hirsch, C., and Serovy, G. K., 1987, "Application of Modified Loss and Deviation Correlations to Transonic Axial Compressors," AGARD, NATO, Neuilly Sur Seine, France, Report No. AGARD-R-745.
[18] Creveling, H. F., and Carmody, R. H., 1968, "Axial Flow Compressor Computer Program for Calculating Off-Design Performance (Program IV)," NASA, Washington, DC, Report No. 19690001542.
[19] Moses, H. L., and Thomason, S. B., 1986, "An Approximation for Fully Stalled Cascades," J. Propul. Power., **2**(2), pp. 188–189.
[20] Moreno, J., Dodds, J., Christopher, S., Zhao, F., and Vahdati, M., 2021, "Aerodynamic Loading Considerations of Three-Shaft Engine Compression System During Surge," ASME J. Turbomach., **143**(12), p. 121002.
[21] Day, I. J., Greitzer, E. M., and Cumpsty, N. A., 1978, "Prediction of Compressor Performance in Rotating Stall," ASME J. Eng. Gas Turbines Power, **100**(1), pp. 1–12.
[22] Emery, J. C., Herrig, L. J., Erwin, J. R., and Felix, A. R., 1958, "Systematic Two-Dimensional Cascade Tests of NACA 65-Series Compressor Blades at Low Speeds," NACA, Washington, DC, Report No. 1368.
[23] Weller, H. G., Tabor, G., Jasak, H., and Fureby, C., 1998, "A Tensorial Approach to Computational Continuum Mechanics Using Object-Oriented Techniques," Comput. Phys., **12**(6), pp. 620–631.
[24] Dumas, M., Vo, H. D., and Yu, H., 2015, "Post-Surge Load Prediction for Multi-Stage Compressors Via CFD Simulations," ASME Paper No. GT2015-42748.
[25] Huang, Q., Zhang, M., and Zheng, X., 2019, "Compressor Surge Based on a 1D-3D Coupled Method–Part 1: Method Establishment," Aerosp. Sci. Technol., **90**, pp. 342–356.
[26] Greenshields, C. J., Weller, H. G., Gasparini, L., and Reese, J. M., 2010, "Implementation of Semi-Discrete, Non-Staggered Central Schemes in a Collocated, Polyhedral, Finite Volume Framework, for High-Speed Viscous Flows," Int. J. Numer. Methods Fluid, **63**(1), pp. 1–21.
[27] Strazisar, A. J., and Powell, J. A., 1981, "Laser Anemometer Measurements in a Transonic Axial Flow Compressor Rotor," ASME J. Eng. Gas Turbines Power, **103**(2), pp. 430–437.
[28] Zhang, W., 2019, "Influence of Inlet Distortion on Fan Aerodynamic Performance," Doctoral dissertation, Imperial College London, London, UK.
[29] Zhang, W., and Vahdati, M., 2019, "Stall and Recovery Process of a Transonic Fan With and Without Inlet Distortion," ASME J. Turbomach., **142**(1), p. 011003.
[30] Sayma, A. I., Vahdati, M., Sbardella, L., and Imregun, M., 2000, "Modeling of Three-Dimensional Viscous Compressible Turbomachinery Flows Using Unstructured Hybrid Grids," AIAA J., **38**(6), pp. 945–954.
[31] Choi, M., and Vahdati, M., 2011, "Recovery Process From Rotating Stall in a Fan," J. Propul. Power, **27**(6), pp. 1161–1168.
[32] Zhao, F., Dodds, J., and Vahdati, M., 2018, "Post-Stall Behavior of a Multistage High-Speed Compressor at Off-Design Conditions," ASME J. Turbomach., **140**(12), p. 121002.
[33] Xu, L., 2003, "Assessing Viscous Body-Forces for Unsteady Calculations," ASME. J. Turbomach., **125**(3), pp. 425–432.
[34] Emmons, H. W., 1955, "Compressor Surge and Stall Propagation," Trans. ASME, **77**(4), pp. 455–467.
[35] Gamache, R. N., and Greitzer, E. M., 1990, "Reverse Flow in Multistage Axial Compressors," J. Propul. Power, **6**(4), pp. 461–473.
[36] Cumpsty, N. A., 2004, *Compressor Aerodynamics*, 2nd ed., Krieger, Malabar, FL.